



HAL
open science

Thermally controlled optical resonator for vacuum squeezed states separation

C. Nguyen, E. Bréelle, M. Barsuglia, E. Capocasa, M.De Laurentis, V. Sequino, F. Sorrentino

► **To cite this version:**

C. Nguyen, E. Bréelle, M. Barsuglia, E. Capocasa, M.De Laurentis, et al.. Thermally controlled optical resonator for vacuum squeezed states separation. *Appl.Opt.*, 2022, 61 (17), pp.5226-5236. 10.1364/AO.459190 . hal-03761660

HAL Id: hal-03761660

<https://hal.science/hal-03761660v1>

Submitted on 1 Mar 2023

HAL is a multi-disciplinary open access archive for the deposit and dissemination of scientific research documents, whether they are published or not. The documents may come from teaching and research institutions in France or abroad, or from public or private research centers.

L'archive ouverte pluridisciplinaire **HAL**, est destinée au dépôt et à la diffusion de documents scientifiques de niveau recherche, publiés ou non, émanant des établissements d'enseignement et de recherche français ou étrangers, des laboratoires publics ou privés.



Distributed under a Creative Commons Attribution 4.0 International License

To be published in Applied Optics:

Title: Thermally-controlled optical resonator for vacuum squeezed states separation

Authors: Catherine Nguyen, Eric Bréelle, Matteo Barsuglia, Eleonora Capocasa, Martina De Laurentis, Valeria Sequino, Fiodor Sorrentino

Accepted: 20 May 22

Posted 24 May 22

DOI: <https://doi.org/10.1364/AO.459190>

© 2022 Optica

OPTICA
PUBLISHING GROUP
Formerly OSA

Thermally-controlled optical resonator for vacuum squeezed states separation

C. NGUYEN,^{1,*} E. BRÉELLE¹, M. BARSUGLIA¹, E. CAPOCASA¹, M. DE LAURENTIS^{2,3}, V. SEQUINO^{2,3}, F. SORRENTINO⁴

¹ *Université de Paris, CNRS, Astroparticule et Cosmologie, F-75006 Paris, France*

² *INFN, Sezione di Napoli, I-80126 Napoli, Italy*

³ *Università di Napoli "Federico II", I-80126 Napoli, Italy*

⁴ *INFN, Sezione di Genova, I-16146 Genova, Italy*

* catherinetrang.nguyen@gmail.com

Abstract: Future gravitational-wave detectors will use frequency-dependent squeezed vacuum states to obtain a broadband reduction of quantum noise. Quantum noise is one of the major limitations to the sensitivity of these detectors. Advanced LIGO+, Advanced Virgo+ and KAGRA plan to generate frequency-dependent squeezed states by coupling a frequency-independent squeezed light state with a filter cavity. An alternative technique is under consideration, based on conditional squeezing with quantum entanglement: the Einstein-Podolsky-Rosen (EPR) squeezing. In the EPR scheme, two vacuum entangled states, the *signal* field at ω_0 and the *idler* field at $\omega_0 + \Delta$ must be spatially separated with an optical resonator and sent to two separate homodyne detectors. In this framework, we have designed and tested a solid Fabry-Perot etalon, to be used in a EPR table-top experiment prototype, thermally controlled without the use of a control probe optical beam. This device can also be used in optical experiments where the use of a bright beam to control an optical resonator is not possible, or where a simpler optical device is preferred.

© 2022 Optical Society of America under the terms of the [OSA Open Access Publishing Agreement](#)

1. Introduction

On September 14, 2015, the first direct detection of gravitational waves (GW) from the merger of two coalescent black holes [1] opened a new window in the observation of the Universe. Since then, the sensitivity of the current interferometric gravitational-wave detectors, Advanced Virgo [2], Advanced LIGO [3], KAGRA [4] and GEO600 [5], has been constantly improved to probe the Universe further and to detect more sources. At the time of writing, about 100 events were observed [6].

A key towards better sensitivity is to reduce quantum noise, which can be seen as the coherent vacuum fluctuations of the optical field entering through the interferometer's dark port. Quantum noise has two components which are driven by phase fluctuations for the *shot noise*, and by amplitude fluctuations for the *radiation pressure noise (RPN)*. The former limits the sensitivity above ~ 100 Hz and the latter is present at lower frequencies [7].

In 1981, C. Caves [8] proposed a method to enhance the current ground-based detectors sensitivity by injecting a squeezed vacuum optical field into the dark port. This squeezed vacuum can be represented by an ellipse, in phase-amplitude space, where the phase uncertainty is reduced with respect to a coherent state, while the amplitude uncertainty is increased. This method, known as *frequency-independent squeezing*, has successfully improved the high-frequency sensitivity in Advanced LIGO [9] and Advanced Virgo [10] by about 3 dB during the last observation run O3, contributing to enlarge the catalog of observed compact binary coalescences [6]. However, due to the Heisenberg Uncertainty Principle, frequency-independent squeezing can only reduce the variance of one quadrature of the optical field at the expense of the other: phase squeezing, i.e. shot noise reduction, corresponds to amplitude anti-squeezing, i.e. RPN enhancement. Up

until the end of O3, shot noise reduction by phase squeezing effectively improved the existing detectors' sensitivity, because RPN was covered by technical noises.

However, after the current upgrades of the interferometric GW detectors, a broadband quantum noise reduction will be necessary, i.e., the squeezing should be frequency-dependent, reducing the fluctuations of each quantum quadrature of the optical field in the frequency band where it is dominant. The solution adopted is to inject the squeezed vacuum into a very long Fabry-Perot cavity, a *filter cavity*. This technique has been already demonstrated [11, 12] and filter cavities of ~ 300 m are being integrated both in Virgo [13] and LIGO detectors [14].

In 2017, Ma and coworkers proposed an alternative using Einstein-Podolsky-Rosen (EPR) entangled states, without the need of an expensive external filter cavity [15]. Because of the reduced cost, complexity and flexibility by not building a long cavity, this technique is very compelling for future detectors as the Einstein Telescope [16]. This proposal relies on the use of the interferometer itself as a filter cavity and has been experimentally demonstrated by two proof-of-principle experiments [17, 18]. With this technique, two EPR-entangled fields, called *signal* and *idler* are injected through the interferometer's output and reflected off from it. Finally, these two fields must be separated before being measured by two separate homodyne detectors. Once the two entangled fields are detected, the rotation of the squeezed vacuum states is achieved by conditionally filtering the measurement.

In this framework, we decided to build a demonstrator [19, 20] to test RPN suppression in a small-scale interferometer (SIPS) [21] with suspended test masses using frequency-dependent squeezing technique with EPR entanglement. This interferometer is limited by RPN in the same frequency band as for GW detectors. This will be a fully automated [22] table-top experiment and will represent a further step towards the injection of EPR squeezing into current GW detectors. In the proposal [15], the EPR-entangled fields are separated with the output-mode cleaner (a resonator) of the interferometer. We chose to use a solid Fabry-Perot etalon, acting as an optical resonator for our demonstrator. This consists of two parallel planar highly-reflective surfaces with a fixed spacing and the cavity between them filled with a solid transparent material, fused silica in our case. The substantial advantage is thus it does not require a bright beam to perform an active length control as for the locking of air-spaced cavities. A temperature feedback system simply controls the cavity length, which enables to physically change the fixed length of this cavity and choose the suitable working condition to transmit the signal field while reflecting the idler field. As a matter of fact, the Fabry-Perot etalon is commonly used to obtain high-resolution spectra in the spectroscopy domain, or used as an optical passive device in optical communications [23] and even in the reduction of coating thermal noise for GW detectors [24]. However, there is very few applications of a thermally-controlled etalon cavity for frequency selection filter purpose.

Here, we present the design and characterization of the first thermally-controlled optical resonator used in an EPR squeezing demonstrator for EPR beams separation. In Section 2, we will describe the optical scheme of this EPR demonstrator. In Section 3, we will give an overview of the design requirements, specifications for the etalon, its mechanical and temperature-controlled system designs. In Section 4, we present the results of the optical characterization and thermal stabilization tests performed in our dedicated characterization bench. It is crucial to evaluate the performances of the etalon as they will impact the measured level of EPR squeezing. Finally, a summary of the work and perspectives are discussed in Section 6.

2. EPR squeezing scheme

Figure 1 shows the simplified optical scheme of our EPR table-top experiment, to test the technique proposed in [15]. First, two EPR-entangled fields are generated using the same components as for the frequency-independent squeezing technique. A main laser pumps a second-harmonic generator (SHG), generating the pump field, at frequency $2\omega_0 + \Delta$, for the

optical parametric oscillator (OPO), which generates the two vacuum entangled fields: the signal field at frequency ω_0 and the idler field at frequency $\omega_0 + \Delta$. The entangled beams are then injected into either a test cavity or the suspended interferometer (SIPS), both mimicking the effect of a GW interferometer. The test cavity and the interferometer arm lengths are controlled to have the signal beam at resonance, while the idler beam, being detuned with respect to the resonance, undergoes a frequency-dependent differential phase rotation, experiencing a quadrature rotation. The two entangled fields, reflected from the cavity or the interferometer arm, are separated and filtered by the etalon and then measured by two separate homodyne detectors. Note that the detection scheme can be different, as shown in [17] where the two entangled beams are directly injected into a bichromatic balanced homodyne detector [25]. However, this technique cannot be applied for GW detectors, as explained in the introduction because of the presence of an output-mode cleaner.

The next section will focus on the separation step which is very important to generate conditional squeezing. The etalon is thus a key element for this technique.

3. Optical resonator specifications and design

In the two proof-of-principle experiments [17, 18], the separation of the entangled fields is made with a triangular stable cavity, similar to the other mode-cleaner cavities used in squeezing experiments. We chose to use a solid Fabry-Perot etalon mainly due to the possibility to simplify as much as possible its alignment and control. First, choosing a very thin cavity makes it less sensitive to the frequency changes of a free-running laser (which is the case for the laser of our test bench). Moreover, the possibility to stabilize the cavity temperature with a simple temperature-controlled system, makes also possible to keep the cavity in its working point without an error signal made with a bright beam, which will greatly simplify the optical scheme of the experiment. A final reason to use an etalon, is to acquire experience with a different method with respect to the ~ 20 cm triangular cavities used in squeezing experiments for other purposes.

We will describe in 3.1 the chosen parameters for the etalon. To ensure a good thermal stabilization, we designed the mechanical holder design and the thermal control system, which are described in 3.3 and 3.4.

3.1. Choice of the thickness and the finesse

The first optical parameter to be defined is the etalon **thickness**. Since the etalon purpose is to separate the two entangled fields (at frequency ω_0 for the signal beam and $\omega_0 + \Delta$ for the idler beam), the etalon **free spectral range (FSR)** is chosen as the double of the entangled beam separation. The signal field will be kept at the cavity resonance while the idler field will be at the cavity anti-resonance (see Figure 2). Since in our experiment $\Delta = 3.8$ GHz, we have:

$$FSR_{etalon} = \frac{c}{2nL_{et}} = 7.6 \text{ GHz} \quad \text{and} \quad L_{etalon} = 13.6 \text{ mm},$$

where L_{et} is the physical length of the etalon and n the refractive index of the material between the reflective surfaces ($n = 1.4496$ for the fused silica), c is the speed of light.

The choice of the **finesse** (and then of the reflectivity of the two etalon surfaces) is dictated by two constraints: the first one is to correctly separate the two beams with the minimum optical losses (as the squeezing is highly impacted by them), and the second one is to allow the simplest possible control of the cavity (and then, have the lowest possible finesse).

The first constraint translates in having the maximum transmission for the signal beam (ω_0), kept at the resonance, and the maximum reflection for the idler beam ($\omega_0 + \Delta$), kept at the anti-resonance.

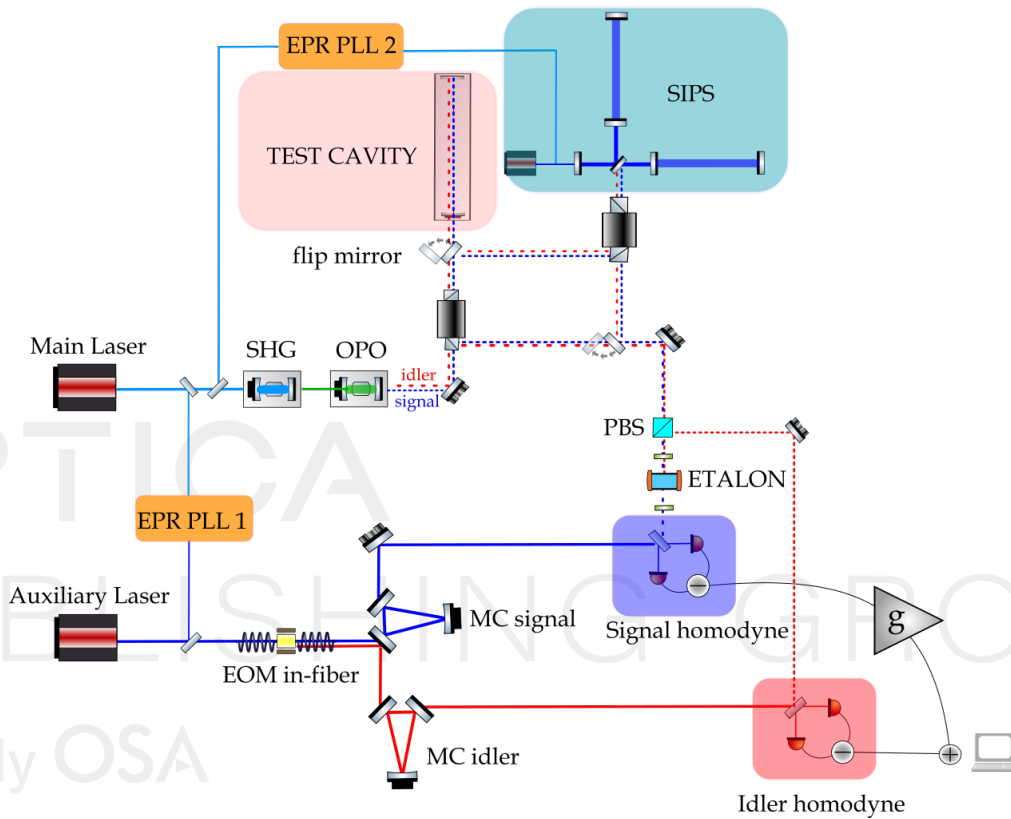


Fig. 1. Simplified optical scheme of our table-top experiment to test frequency-dependent squeezing using EPR entanglement. The entangled signal (blue) at ω_0 and idler (red) fields at $\omega_0 + \Delta$, are generated by the OPO, as for a frequency-independent squeezing experiment. They are injected into either a test cavity which mimics an interferometer arm or either the SIPS. Then the reflected beams are spatially separated by the etalon using a polarization filtering (the transmitted signal field and reflected idler field have perpendicular linear polarization). The two entangled fields are then measured by two separate homodyne detection systems and are electronically recombined using an optimal filter (with a gain g) for the final readout measurement. The abbreviations PBS, MC, SHG, OPO and PLL stand respectively, for polarizing beam-splitter (PBS), mode-cleaner, second-harmonic generator, optical parametric oscillator and phase locked-loop.

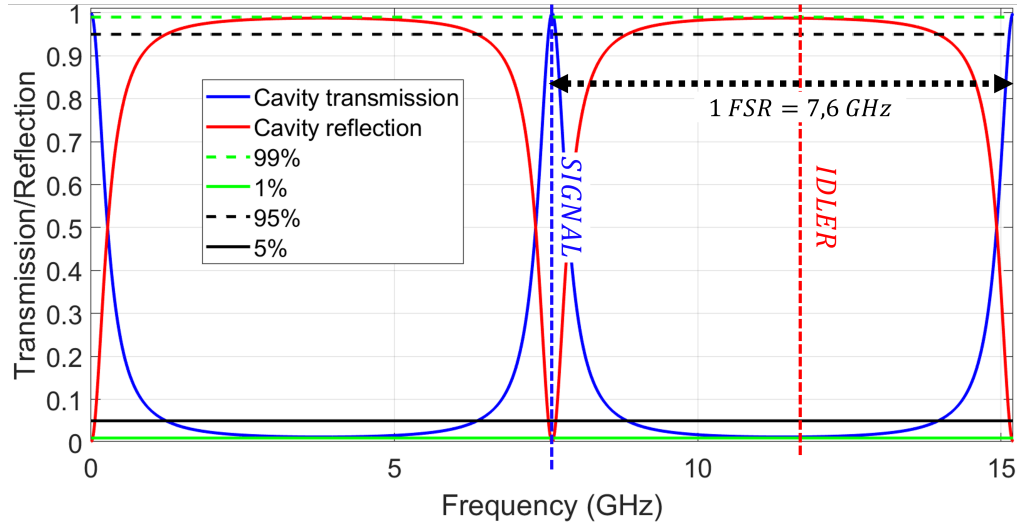


Fig. 2. Transmission and reflection of the etalon, the signal (dotted-blue) and idler (dotted-red) frequencies with respect to the resonance and anti-resonance of the cavity are indicated. The limits at 1%, 5%, 95% and 99% are also indicated.

The etalon is a resonant cavity that is characterized by transmission resonances varying periodically, due to the interferences between multiple reflections of light inside it. The expression of the transmitted field of the cavity (normalized with respect to the input beam) is:

$$T_{cav}(\Phi) = \left(1 - \frac{A}{1 - \mathcal{R}}\right)^2 \frac{1}{1 + (2\mathcal{F}/\pi)^2 \sin^2(\phi(f)/2)},$$

where $\mathcal{R} = r^2$ considering the same amplitude reflectivity r for the two surfaces, A is the round trip losses. The finesse \mathcal{F} (for a very high amplitude reflectivity) and the round-trip phase $\phi(f)$ are defined as:

$$\mathcal{F} = \frac{\pi\sqrt{\mathcal{R}}}{1 - \mathcal{R}} \simeq \frac{\pi}{1 - \mathcal{R}}, \quad \phi(f) = \frac{4\pi n L_{et} f}{c}.$$

The round-trip losses A can be estimated from the surface roughness σ and the total loss A_{tot} can be expressed as:

$$A = 2 \left(\frac{2 * \pi \sigma}{\lambda} \right)^2, \quad A_{tot} \simeq \frac{2A}{1 - \mathcal{R}} \simeq \frac{2A\mathcal{F}}{\pi}. \quad (1)$$

Considering a roughness of 0.5 nm, this gives a total round trip loss of $A \simeq 70$ ppm, which will be approximated, in a conservative way, to 100 ppm for the design phase. A_{tot} is thus equal to $64 \times \mathcal{F}$ ppm. This means that $A_{tot} \geq 1\%$ for $\mathcal{F} \geq 156$.

Figure 3 shows the transmitted and reflected idler and signal fields as a function of the finesse and the amplitude reflectivity r . As calculated earlier, to reach a signal field transmitted at more than 99% the finesse should be less than 150. Otherwise, the round-trip losses are not negligible anymore. To achieve an idler field reflected at more than 99%, the finesse should be higher than ~ 14 . To conclude, to have less than 1% of losses for the signal and idler beam, the possible range for the finesse is between 14 and 150 and for the limit at 95%, the possible range is between 6 and 780.

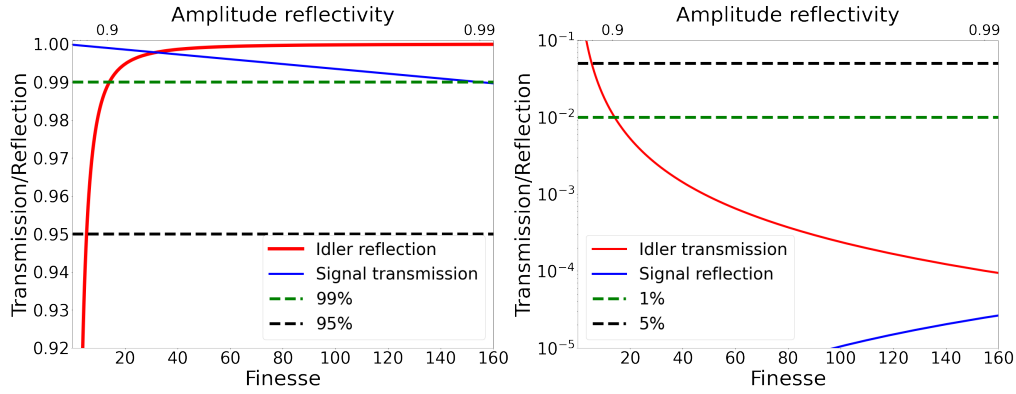


Fig. 3. Transmission and reflection of the idler and signal fields as a function of the finesse and the amplitude reflectivity r . **(Left)** Idler reflection (in red) and signal transmission (in blue) along with the requirement curves at 95% (in black-dotted) and 99% (in green-dashed). **(Right)** Idler transmission (in red) and signal reflection (in blue) along with the requirement curves at 5% (in black-dotted) and 1% (in green-dotted).

Considering this range, we chose the lowest possible finesse ($\mathcal{F} = 14$) in order to release as much as possible the requirements on the cavity control, then to have a less stringent constraint in the stability of the temperature and a less sensitivity with respect to the frequency noise and drifts.

Let us also remark that the requirements of 95% for the signal transmission and 5% for the idler reflection are preliminary requirements, aiming to minimize the readout losses [26] which can degrade the squeezing level.

3.2. Cavity control simulations: temperature stability and frequency noise

After choosing a **finesse of 14**, we have considered two main perturbations for the control of the cavity: the temperature variations of the etalon and the frequency drift of the laser. By neglecting the term $O(\Delta T^2)$ and considering that the etalon is at resonance for $\Delta T = 0$, the temperature affects the transmission and reflection of the etalon as follows:

$$\phi(f, \Delta T) \simeq \frac{4\pi n f L_{et}}{c} \left(\frac{dn}{dT} \Delta T + \alpha \Delta T \right), \quad (2)$$

where $\alpha = 0.55 \times 10^{-6} \text{ } ^\circ\text{C}^{-1}$ is the fused silica thermal expansion coefficient (for Suprasil fused silica) and $\frac{dn}{dT} = 0.87 \times 10^{-5}$ the change in the refractive index with temperature [27].

Considering the **temperature stability of the etalon**, Figure 4 (left) shows the transmission of the signal beam as a function of the temperature variation of the etalon and of the finesse, for 100 ppm round trip losses. A similar calculation was done with the idler field reflection at the anti-resonance condition, but the resulting tolerance is much looser than the one for signal transmission. On the other hand, Figure 4 (right) shows the transmission of the signal field for a finesse of 14. We see that in order to guarantee a transmission of 99% we need a stability of $\sim 0.01 \text{ } ^\circ\text{C}$ and for a transmission of 95% we need a stability of $0.025 \text{ } ^\circ\text{C}$. Consequently, for the thermal control system described in 3.4, the specification to take into account is that the temperature fluctuations have to be smaller than $\pm 0.01 \text{ } ^\circ\text{C}$. Considering variations of the room temperature of the order of half a degree, this means that we need a temperature stabilization to keep the etalon in resonance with the laser light.

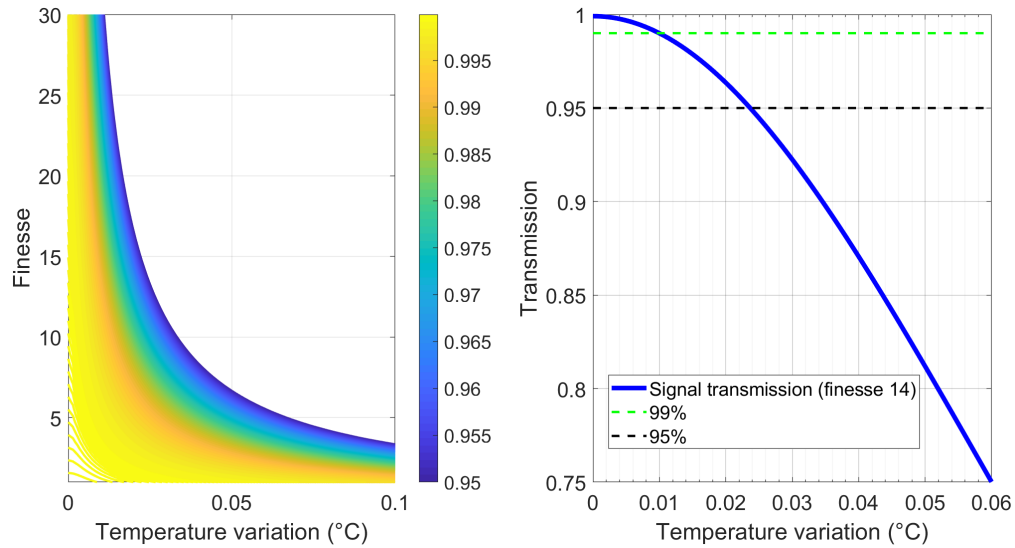


Fig. 4. **(Left)** Transmission of the signal field at the resonance condition in function of the temperature variation and the finesse. **(Right)** Signal transmission as a function of temperature variation for a finesse of 14 along with the requirement level at 95% (black-dotted) and 99 % (green-dotted).

A similar simulation is done to study the influence of the **frequency drift** on the cavity transmission. Considering that the etalon is at resonance for $\Delta f = 0$, the frequency drift affects the transmission and reflection of the etalon as follows:

$$\phi(\Delta f) \simeq \frac{4\pi n L_{et} \Delta f}{c}$$

To have a transmission higher than 99%, the frequency should not change more than 25 MHz. The lasers Mephisto and Mephisto S from Coherent company [28] used in our experiments, have a long term drift of the order of 5 MHz, therefore the laser drifts, due to the cavity small thickness, will not put the cavity out of resonance.

3.3. Mechanical holder design

The strategy for scanning and stabilizing the etalon temperature to find the working condition is to use a Peltier element (thermoelectric cooler). We decided to design a mechanical holder with the Peltier element glued at the top of it. The topology of the holder should ensure a good thermal contact with the etalon. Indeed, when a temperature change is induced by the Peltier element, the heat from the Peltier element should be transferred homogeneously to the whole etalon.

We chose to ask SLS Optics for the fabrication of the etalon. The properties ensured by the manufacturer, are described in Table 1.

As depicted in Figure 5, an indium foil wraps the etalon lateral side, to ensure a good thermal contact with the holder. The bottom part of the holder (in yellow in the drawing) is in acrylonitrile butadiene styrene (ABS), a durable plastic to prevent from thermal cut-off with the optical table. Two thermistors are used: an *in-loop thermistor* (model TCS10K5) which is used for the PID control and an *out-of-loop thermistor* (model TCS610), which is used as a temperature witness.

3.4. Temperature-controlled system

The temperature controlled system have to enable to scan enough range of temperature to find the working point and then, stabilize in a long-term duration at this temperature with a maximum

Manufacturer	SLS Optics Ltd.
Etalon thickness	13.604 mm
Clear aperture	28.0 mm
FSR	7.6 GHz
Finesse	14
Reflector coating	80.0 %
Surface roughness	0.44 nm RMS

Table 1. Design parameters provided by the manufacturer.

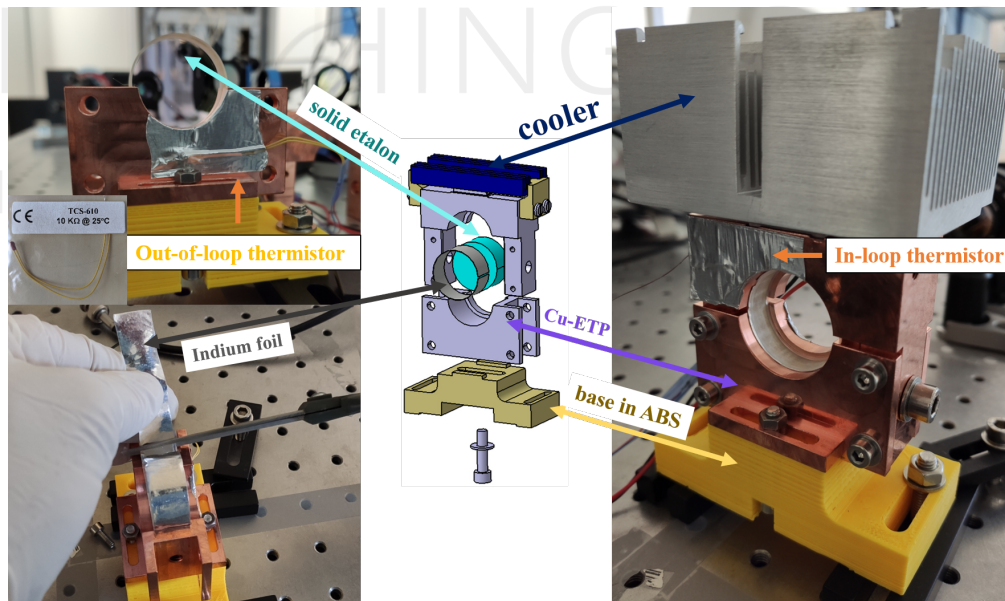


Fig. 5. An exploded view of the mechanical design of the etalon holder along with photographs of the etalon in its holder, with the thermistors glued on the holder with thermal tape.

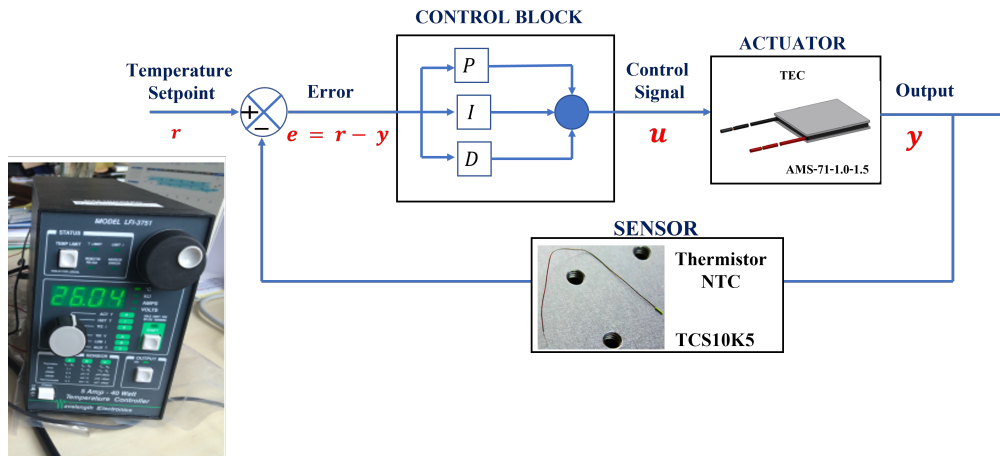


Fig. 6. Representation of the temperature feedback control system along with photographs of the temperature controller, the in-loop thermistor (model TCS10K5) as the sensor and the Peltier element (model AMS-71-1.0-1.5) as the actuator.

range of temperature fluctuations of ± 0.01 °C. Since the temperature of the room can change by half a degree or more, we need a feedback system, to keep the temperature of the etalon constant. The feedback system is represented in Figure 6, in a block diagram. $e = r - y$ is the *control error*, equal to the difference between the reference signal (or also called the *setpoint*) r and the output of the system y , u is the actuation command. There are three main components in such a system: the temperature sensor (the *in-loop thermistor*), the temperature controller (model LFI-3751 from Wavelength Electronics [29]) and a Peltier device (model AMS-71-1.0-1.5 [30]).

4. Experimental setup

The characterization of the whole etalon system (etalon installed in its mechanical holder with its thermal control system) has been done in a cleanroom of Class ISO 08 at the APC laboratory.

4.1. Description of the setup

As depicted in Figure 7, a Nd:YAG at 1064 nm (a Mephisto S laser [28]) provides a p-polarized beam and the half-wave plate "HWP_2" is tuned so that there is a s-polarized incident beam part that arrives at "PD_in" (see Figure 12). Before being injected, the beam is going through a PBS, then a quarter-wave plate (QWP, called "QWP_2" in the figure). If the beam is reflected back by the etalon, it will undergo a second time through the same QWP and it will become s-polarized. This beam will arrive back to the polarizing beam splitter that will reflect this beam in the "reflection detection arm". If the beam is transmitted by the etalon, it will go through a second QWP ("QWP_3") that will turn the polarization from circular to linear. For each detection arm, the beam is detected by a photodiode and also imaged by a camera. The orange area indicates the zone covered by an insulated box in polystyrene. This will ensure better temperature stabilization but is not necessary to reach the requirements.

Concerning the matching of the beam to the etalon, a simulation was performed with a software called *GaussianBeam* [31]. We modelled the beam with parameters as the waist and position of the input beam, the position of lenses and their focal length and access at every position to the beam parameters such as its radius. This enables to have a collimated beam (after choosing the adapted lens) arriving on the etalon, with the adapted waist, which should be higher than around 340 μm , to not degrade the etalon performances. This waist was calculated based on the

manufacturer specification of having a divergence angle smaller than 1 mrad for the beam, to keep the transmission and reflection higher than 95%.

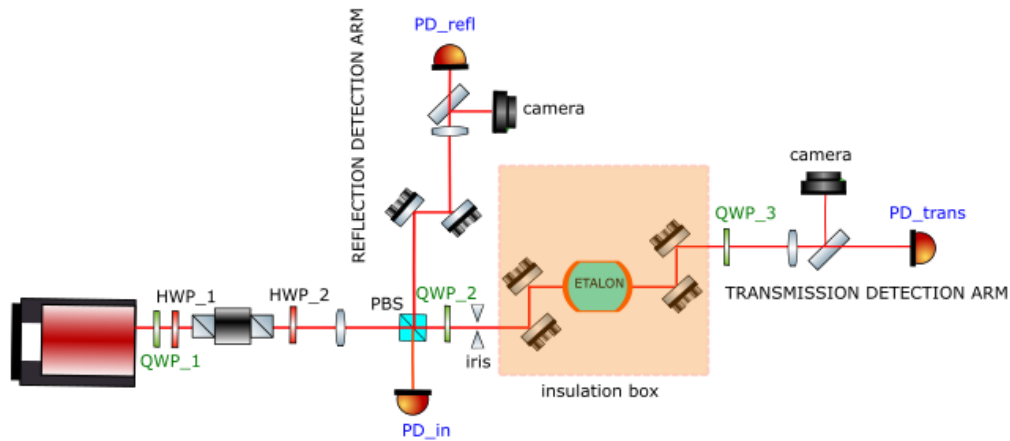


Fig. 7. Schematics of the characterization bench for etalon tests. A Nd:YAG at 1064 nm provides a p-polarized beam which is injected through the etalon. Thanks to the combination of a PBS and a QWP ("QWP_2"), a polarization discrimination enables to spatially separate the reflected beam from the etalon and the transmitted beam. Each beam is detected separately with its dedicated photodiode and camera. The orange area indicates the zone covered by an insulated box in polystyrene.

5. Experimental results

The experimental results will be divided into two categories: optical characterization and thermal stabilization. The aims of the optical characterization are to evaluate the separation power of the etalon and the conservation of the TEM_{00} mode for both transmitted and reflected beam. The aim of the thermal stabilization part is to evaluate the efficiency of the thermal stabilization to keep the cavity in resonance with the laser light.

5.1. Optical characterization

The optical characterization is separated into two axes. First, it is composed of the determination of the etalon finesse and the evaluation of the resonant (respectively, off-resonant) transmission and reflection efficiencies. The second axis consists of the overlap integral calculation, designed for evaluating the purity of the TEM_{00} mode (fundamental mode). In the homodyne detection principles, the detected beam beats with a beam called local oscillator (LO) that is, in our case, a beam at TEM_{00} mode. If the beams separated by the etalon do not have the same spatial mode as their corresponding LO beams, the detection is degraded, thus the squeezing level measured is lowered.

5.1.1. Finesse and efficiency

To measure experimentally the finesse of the etalon, we acquire the power of the transmitted and reflected fields with the photodiodes PD_{trans} and PD_{refl} (see Figure 7) while scanning the laser frequency in a range where the etalon is resonant and off-resonant, through a scan in temperature of the laser crystal and then we perform a fit of the transmitted power. A typical curve obtained during the scan is shown by Figure 8 (right), where the y-axis is normalized to the incident power and the laser frequency absolute values are shifted so that the frequency of the transmission peak is equal to one FSR (7.6 GHz).

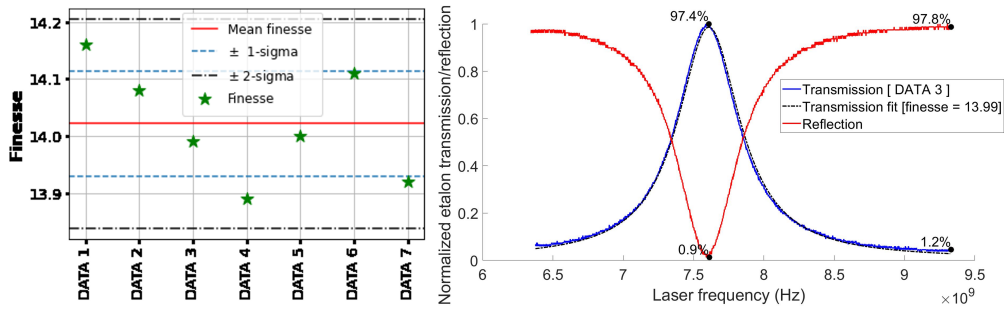


Fig. 8. **(Left)** Plot of 7 different fits of finesse along with its statistic mean equal to 14.02, its 1-sigma and 2-sigma intervals. **(Right)** Normalized transmission and reflection vs. frequency from DATA 3: etalon transmission curve (blue) along with its fit curve (black-dotted), etalon reflection curve (red) and the transmission and reflection values at resonance and anti-resonance. For ease of visualization for the x-axis units, the curves are shifted in frequency so that the frequency of the transmission peak is equal to one FSR (7.6 GHz).

	Transmission (%)	Reflection (%)
Resonance	97.4	0.9
Out of resonance	1.2	97.8

Table 2. Measured transmission and reflection values when the etalon is resonant and off-resonant

For the reflection part, the reflected beam power can only be measured in the path to the reflection arm, just after the PBS. The propagation losses from the etalon to the PBS were estimated to subtract these losses in our measures. At the resonance condition, the transmission is equal to 97.4% while the reflection is equal to 0.9%. At the anti-resonance condition, the transmission is equal to 1.2% while the reflection is equal to 97.8%. These values, presented in Table 2 meet our specifications of having more than 95% for signal transmission and idler reflection. According to Figure 8 (left), the measured finesse is 14.02 with a standard deviation (calculated from the seven data) of ± 0.08 , the finesse quoted by the manufacturer being inside this interval.

5.1.2. Overlap integral

The detection technique requires to couple each EPR-entangled beam with a local oscillator beam which has the same properties as the interferometer beam and particularly, being at TEM_{00} mode. The Figures 9, 10 and 11 (left) show the images of the input field and the transmitted and reflected field from the etalon. We notice some interference fringes, which are probably made by some optical components on the beam path. However, it was possible to remove offline these fringes by applying a low-pass filter to the FFT of each image but we notice that the calculated *overlap integral* (defined later) is the same, with or without these fringes. The figures at the right side are the corresponding fit of each image with a TEM_{00} intensity profile.

We use an *intensity overlap integral* to measure the purity of the transmitted and reflected modes. The overlap integral is made with a perfect TEM_{00} beam which has the same radius of the measured field, and which is defined as:

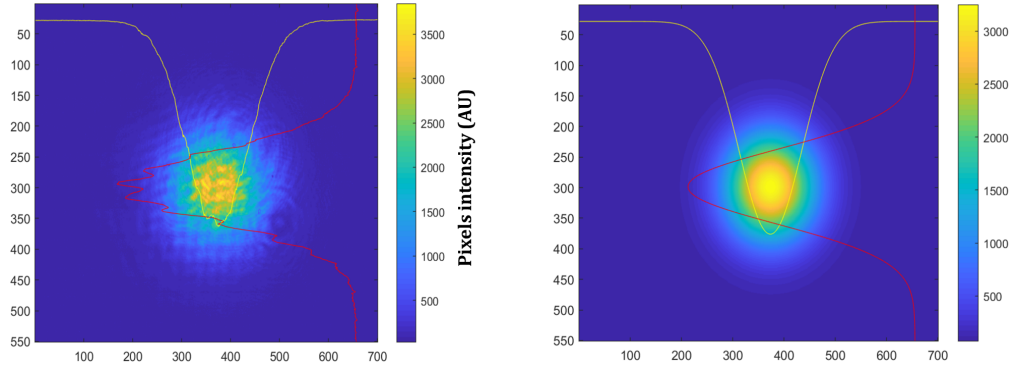


Fig. 9. **(Left)** Image of the input beam captured by the beam profiler at about 75 mm before the etalon, plotted along with its averaged horizontal and vertical profiles (scaled to fit in the picture) **(Right)** Fit of the input beam with a TEM_{00} intensity profile, plotted along with the averaged horizontal and vertical profiles.

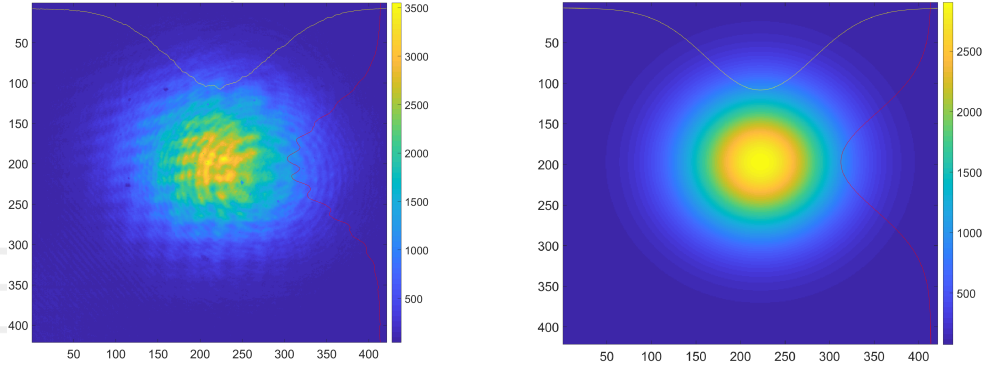


Fig. 10. **(Left)** Image of the transmitted beam captured by the beam profiler at about 75 mm after the etalon, plotted along with its averaged horizontal and vertical profiles (scaled to fit in the picture) **(Right)** Fit of the transmitted beam with a TEM_{00} intensity profile, plotted along with the averaged horizontal and vertical profiles.

$$\gamma_{mes,th} = \frac{|\sqrt{I_{mes}} \times \sqrt{I_{theory}} \exp(i\Delta\Phi)|^2}{\iint I_{mes} dS \times \iint I_{theory} dS}, \quad (3)$$

where I_{mes} is the transverse intensity distribution acquired by a beam profiler camera, I_{theory} is the numerical fit (nonlinear curve-fitting in a least-square sense) of the transverse intensity distribution of the image from the beam profiler with a perfect Gaussian intensity distribution, dS is the infinitesimal surface element and $\Delta\Phi$ is the differential of the two phase profiles. However, since it is more complex to measure the phase of a laser beam as it cannot be measured by a beam profiler but it requires a wavefront sensing device, we will assume $\Delta\Phi$ equals zero (i.e., the two profiles are perfectly marched). Hence we can only obtain an upper limit for $\gamma_{mes,th}$. The numerical integration for the Equation 3 becomes:

$$\gamma_{mes,th} = \frac{\sum_{x=1}^n \sum_{y=1}^m I_{mes}(x, y) I_{th}(x, y) \Delta x \Delta y}{\sqrt{\sum_{x=1}^n \sum_{y=1}^m I_{mes}^2(x, y) \Delta x \Delta y} \sqrt{\sum_{x=1}^n \sum_{y=1}^m I_{th}^2(x, y) \Delta x \Delta y}}, \quad (4)$$

where I_{mes} is the image from the beam profiler at the size $n \times m$ pixels, x and y are the indexes in

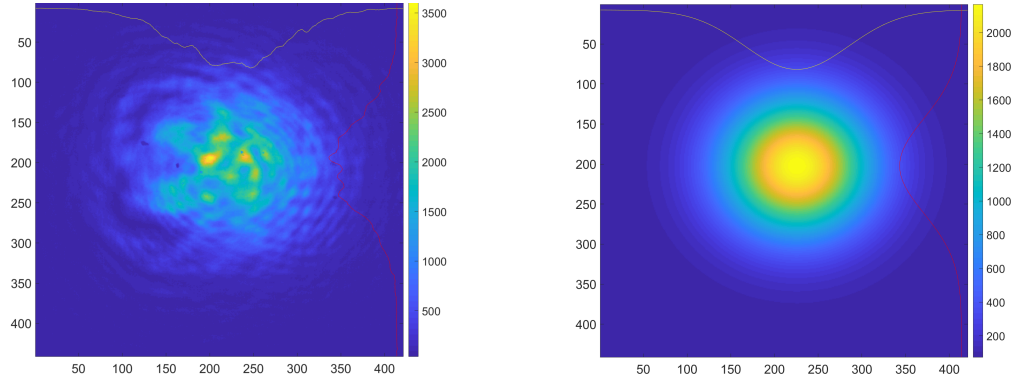


Fig. 11. **(Left)** Image of the reflected beam captured by the beam profiler at about 450 mm in the reflected path from the etalon, plotted along with its averaged horizontal and vertical profiles (scaled to fit in the picture) **(Right)** Fit of the reflected beam with a TEM_{00} intensity profile, plotted along with the averaged horizontal and vertical profiles.

horizontal and vertical direction, Δx and Δy are the increment steps in respectively the horizontal and vertical direction and are equal to the size of one pixel. I_{th} is the fit image. The nonlinear function to fit is:

$$F(X, Y) = ae^{-2\frac{(X-b)^2+(Y-c)^2}{\sigma^2}},$$

where a is the intensity normalization coefficient, b and c are the shift of the intensity peak for the vertical and horizontal direction and σ is proportional at the Full-Width at Half Maximum (FWHM) of the function with $\sigma = \frac{FWHM}{\sqrt{2\ln 2}}$ or can be defined as the radius for which the intensity is equal to the maximum intensity times $1/e^2$.

The resulting overlap integral is equal to 99.2% for the incident beam, 99.3% for the transmitted beam and 96.9% for the reflected beam. The result for the reflected beam is slightly worse than the other results, what may come from a residual tilt angle of the incidence beam.

5.2. Thermal stabilization tests

Tests were performed to evaluate our temperature controller performances and to choose the PID experimentally to minimize the time needed for the etalon to be stabilized at the set temperature.

In the following subsections, we present a long-term stabilization measurement taken with the etalon in resonance condition; the temperature of the etalon is stabilized, the etalon and its four steering mirrors are placed inside an insulated box, as shown by the orange area in Figure 7. The measurement is done in a period of more than 22-hour with the acquisition of the incident, transmission and reflection voltages, the room temperature, the temperature inside the insulated box, the in-loop and out-of-loop temperature. The *Agilent 34970A Data Logger Switch Unit* acquires the three photodiodes (reference: Thorlabs PDA36A-EC, Si Amplified Detector) PD_{trans} , PD_{refl} and PD_{in} and the sampling rate is 0.1 Hz. This data logger also acquires the temperatures from the out-of-loop thermistor and the room temperature thermistor. The temperature controller acquires the temperatures from the in-loop thermistor for the PID stabilization and from the thermistor placed inside the insulated box, with a sampling rate of 0.2 Hz.

5.2.1. Transmission evolution

After observing that the transmission fluctuations follows the fluctuations of the incident power, we removed the effect of laser intensity fluctuations thanks to the acquisition of the fluctuations of the incident power (easily calculated thanks to the acquisition of the photodiode PD_{in} which acquires a pick-up beam from the laser). T_{cav} is then the transmission function whose values are between 0 and 1 and is shown by Figure 12.

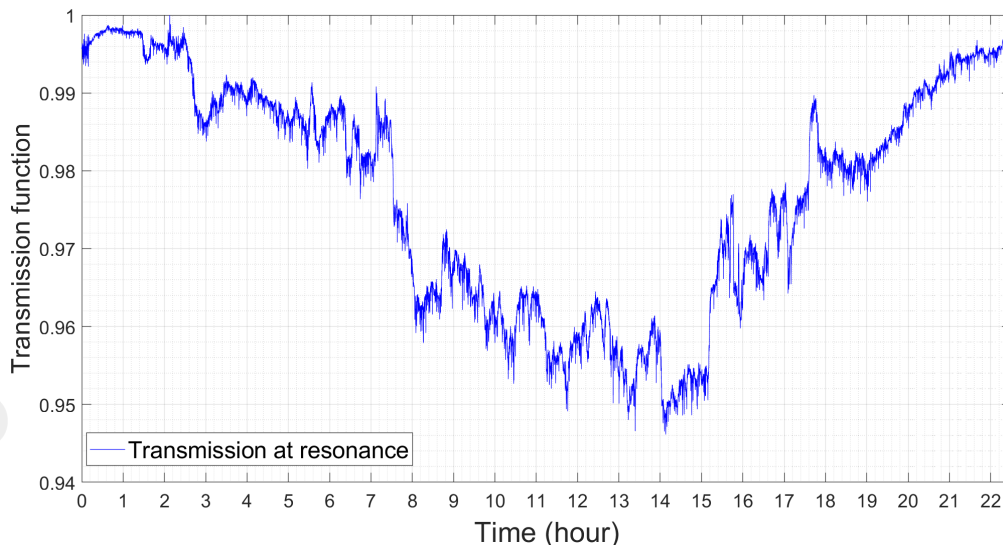


Fig. 12. More than 22-hour acquisition of the transmission function (transmission power normalized with the incident power) with the etalon in resonance condition.

The variations in the transmission curve seem to follow a cycle, the transmission decreases during the first 15 hours and drops to 95% and then, it increases to reach more than 99% of transmission again. In a one-day period, the transmission stays at higher than 95%. Moreover, the reflection (which is not plotted for ease of visualization) is never higher than 2% during the whole measurement period.

5.2.2. Temperatures evolution

The *Agilent 34970A Data Logger Switch Unit* acquires the temperatures from the out-of-loop thermistor and the room temperature thermistor. The temperature controller acquires the temperatures from the in-loop thermistor and the thermistor placed inside the insulated box. In Figure 13, the evolution on a 22-hour period of the four temperatures is plotted. The fluctuations in 22 hours for the in-loop and out-of-loop temperature are respectively $\pm 0.0025^\circ\text{C}$ and $\pm 0.007^\circ\text{C}$. The in-loop temperature and insulated box data are down-sampled, to have the same sampling for the four temperature curves. We can observe that the in-loop and out-of-loop temperatures are very stable compared to the room temperature and the insulated box temperature and the zoom in a 1-hour period, depicted in Figure 14, shows that their fluctuations are respectively $\pm 0.0005^\circ\text{C}$ and 0.001°C . Moreover, the model of all the thermistors is TCS610, except the one for the in-loop temperature (model TCS10K5). Thus, the big fluctuations in the room temperature cannot be caused by the difference in thermistors performances between different models. They are certainly due to the room temperature itself and not from the numerical noises of the thermistor. The presence of the insulated box made the temperature inside it increase, this explains the increase of the related measure (red trace in Figure 13) during the first five hours.

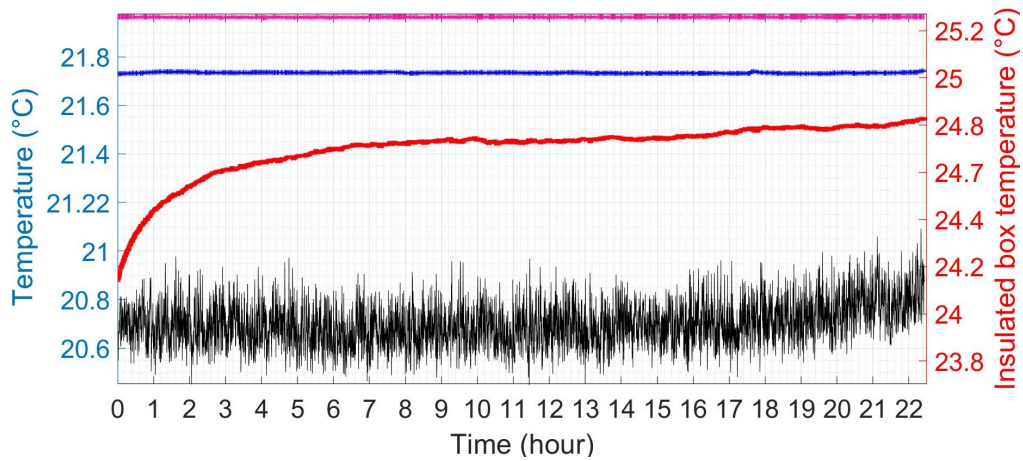


Fig. 13. Evolution of the different acquired temperatures on more than 22 hours: in-loop (pink) and out-of-loop (blue) temperatures, room temperature (black) and insulated box (red). The fluctuations during all this period for the in-loop and out-of-loop temperature are respectively $\pm 0.0025\text{ }^{\circ}\text{C}$ and $\pm 0.007\text{ }^{\circ}\text{C}$.

OPTIK
PUBLISHING GROUP
Formerly OSA

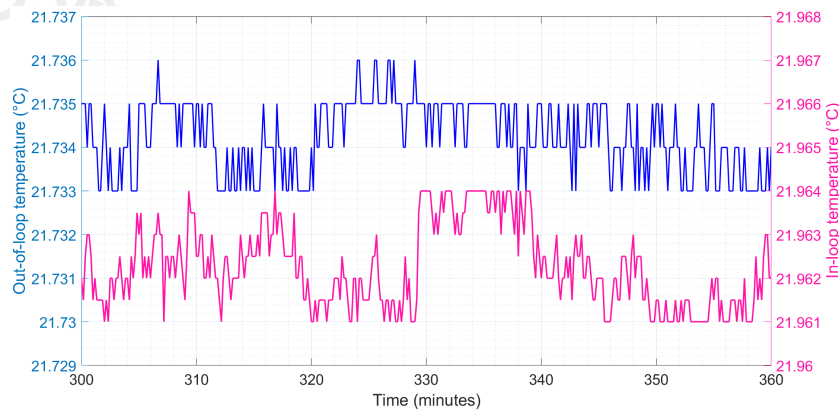


Fig. 14. Zoom in a 1-hour period for the in-loop and out-of-loop temperatures, to see the fluctuations. Note that the two y-axes are shifted towards each other but the scale is the same.

5.2.3. Discussion on stabilization tests

The long-term stabilization measurement shows that the signal transmission can be kept higher than 95% during at least one day. The temperature, measured with an out-of-loop sensor was stable at 0.001 °C on 22-hour and 5 times better on a 1-hour period. The conclusion is that the variations of the transmission signal cannot be explained only by a change of length in the etalon but there are other factors (alignment drifts or change in the frequency of the laser higher than expected).

6. Conclusions and outlook

We have made the design and tested a separation cavity for the EPR experiment, based on a Fabry-Perot etalon. The whole system was installed in a characterization setup in cleanroom to test its optical properties and its thermal stabilization system. Concerning the optical characterization, a finesse of 14 ± 0.08 and an overlap integral $> 97\%$ for the transmitted and reflected beam was determined. These results guarantee respectively a good beam separation and a reasonable level of losses for homodyne measurements. The transmission of the signal and reflection of the idler beams are almost equal to 98%, which meets our specification of 95%. This will guarantee to reduce losses due to readout loss for the production of EPR squeezing. Indeed, as explain in [ref thesis], it is possible to link the variance of produced squeezing level and the measured variance with:

$$V^{meas} = \eta_{tot} V^{prod} + (1 - \eta_{tot}) \quad (5)$$

where V^{meas} and V^{prod} are respectively the measured squeezing variance and the produced squeezing variance, and η_{tot} is the total optical efficiency that includes all the losses L from the generation to the detection of squeezed light and these follows the relation $\eta_{tot} = 1 - L$. Considering only the losses from the etalon, $\eta_{tot} = 0.97 * 0.97$, which are the measured transmission for the signal beam and the measured reflection for the idler beam, with a produced squeezing level goal of -15 dB, we should have a measured squeezing level of -10.5 dB, which is detectable. For our demonstrator, the goal is to be able to produce and measure EPR squeezing and understand all the losses.

The short-term and long-term stability of the temperature-controlled system show temperature fluctuations around ± 0.0005 °C on 1-hour time scale and ± 0.0025 °C on 22-hour time scale. This is respectively 20 times and 4 times smaller than the requirement. The stabilization on a 1-hour and a 22-hour scale thus meet the requirement on the temperature fluctuations.

From these tests, we can conclude that our etalon is ready to be integrated in the EPR experiment: the whole etalon system is a robust and stable optical element for the purpose of EPR beams separation in a frequency-dependent squeezing experiment using quantum states entanglement. For further characterizations, it would be important to do more extensive tests to understand the effects of the misalignments of the incident beam and compare the results with simulations.

Funding. Italian Istituto Nazionale di Fisica Nucleare (INFN) and EGO consortium.

Acknowledgment. The authors gratefully acknowledge the Italian Istituto Nazionale di Fisica Nucleare (INFN) for financial support, and the French Centre National de la Recherche Scientifique (CNRS) for the creation and support of the EGO consortium together with INFN. C. Nguyen acknowledges the EGO consortium for financial support during this work. F. Sorrentino and V. Sequino acknowledge the Italian Ministry of Education, University and Research (MIUR) for financial support under the PRIN project 2015L33WAK_002. We would like to thank Jean-Pierre Baronick, Pierre Prat and Stéphane Dheilily for their contribution to the experimental apparatus and the Virgo EPR squeezing team for useful discussions.

Disclosures. The authors declare no conflicts of interest.

Data availability. Data underlying the results presented in this paper are not publicly available at this time but may be obtained from the authors upon reasonable request.

References

1. B. P. Abbott, R. Abbott, T. D. Abbott *et al.*, “Observation of gravitational waves from a binary black hole merger,” *Phys. review letters* **116**, 061102 (2016).
2. F. Acernese, M. Agathos, K. Agatsuma *et al.*, “Advanced Virgo: a second-generation interferometric gravitational wave detector,” *Class. Quantum Gravity* **32**, 024001 (2014).
3. J. Aasi, B. P. Abbott, R. Abbott *et al.*, “Advanced LIGO,” *Class. Quantum Gravity* **32**, 074001 (2015).
4. T. Akutsu, M. Ando, A. Araya *et al.*, “The status of KAGRA underground cryogenic gravitational wave telescope,” *J. Physics: Conf. Ser.* **1342**, 012014 (2020).
5. K. L. Dooley and (for the LIGO Scientific Collaboration), “Status of GEO 600,” *J. Physics: Conf. Ser.* **610**, 012015 (2015).
6. The LIGO Scientific Collaboration, the Virgo Collaboration, and the KAGRA Collaboration, “GWTC-3: Compact Binary Coalescences Observed by LIGO and Virgo During the Second Part of the Third Observing Run,” arXiv 2111.03606 (2021).
7. H. J. Kimble, Y. Levin, A. B. Matsko, K. S. Thorne, and S. P. Vyatchanin, “Conversion of conventional gravitational-wave interferometers into quantum nondemolition interferometers by modifying their input and/or output optics,” *Phys. Rev. D* **65**, 022002 (2001).
8. C. M. Caves, “Quantum-mechanical noise in an interferometer,” *Phys. Rev. D* **23**, 1693–1708 (1981).
9. M. Tse, H. Yu, N. Kijbunchoo *et al.*, “Quantum-Enhanced Advanced LIGO Detectors in the Era of Gravitational-Wave Astronomy,” *Phys. Rev. Lett.* **123**, 231107 (2019).
10. F. Acernese, M. Agathos, L. Aiello *et al.*, “Increasing the Astrophysical Reach of the Advanced Virgo Detector via the Application of Squeezed Vacuum States of Light,” *Phys. Rev. Lett.* **123**, 231108 (2019).
11. Y. Zhao, N. Aritomi, E. Capocasa *et al.*, “Frequency-Dependent Squeezed Vacuum Source for Broadband Quantum Noise Reduction in Advanced Gravitational-Wave Detectors,” *Phys. Rev. Lett.* **124**, 171101 (2020).
12. L. McCuller, C. Whittle, D. Ganapathy, K. Komori, M. Tse, A. Fernandez-Galiana, L. Barsotti, P. Fritschel, M. MacInnis, F. Matichard, K. Mason, N. Mavalvala, R. Mittleman, H. Yu, M. E. Zucker, and M. Evans, “Frequency-Dependent Squeezing for Advanced LIGO,” *Phys. Rev. Lett.* **124**, 171102 (2020).
13. The Virgo Collaboration, “VIR-0596A-19 Advanced Virgo Plus Phase I - Design Report,” (2019).
14. The LIGO Scientific Collaboration, “Instrument Science White Paper 2020,” T2000407-v3.
15. Y. Ma, H. Miao, B. H. Pang, M. Evans, C. Zhao, J. Harms, R. Schnabel, and Y. Chen, “Proposal for gravitational-wave detection beyond the standard quantum limit through EPR entanglement,” *Nat. Phys.* **13**, 776–780 (2017).
16. P. Jones, T. Zhang, H. Miao, and A. Freise, “Implications of the quantum noise target for the Einstein telescope infrastructure design,” *Phys. Rev. D* **101** (2020).
17. J. Südbeck, S. Steinlechner, M. Korobko, and R. Schnabel, “Demonstration of interferometer enhancement through Einstein–Podolsky–Rosen entanglement,” *Nat. Photonics* **14**, 240–244 (2020).
18. M. J. Yap, P. A. Altin, T. Mcrae, B. J. J. Slagmolen, R. L. Ward, and D. McClelland, “Generation and control of frequency dependent squeezing via EPR entanglement,” (2020).
19. V. Sequino and (for the Virgo Collaboration), “EPR experiment for a broadband quantum noise reduction in gravitational wave detectors,” in *Proceedings of GRAvitational-waves Science & technology Symposium*, (2019).
20. C. Nguyen, “Development of squeezing techniques for quantum noise reduction in gravitational-wave detectors,” Ph.D. thesis, Paris university (2021).
21. L. Giacoppo, E. Majorana, S. D. Pace, L. Naticchioni, M. D. Laurentis, V. Sequino, M. Bawaj, F. Ricci, P. Puppo, P. Rapagnani, F. Sorrentino, F. Travasso, A. Pasqualetti, M. Perciballi, G. Cella, F. Frasconi, A. F. Piluso, and A. Basti, “Towards ponderomotive squeezing with SIPS experiment,” *Phys. Scripta* **96**, 114007 (2021).
22. C. Nguyen, M. Bawaj, V. Sequino *et al.*, “Automated source of squeezed vacuum states driven by finite state machine based software,” *Rev. Sci. Instruments* **92**, 054504 (2021).
23. L. Ren, Y. Li, Q. Wang, B. Lu, Y. Qiu, B. Mao, and H. Li, “Study of temperature controlling of a solid Fabry–Pérot etalon,” in *Proceedings of 18th International Conference on Optical Communications and Networks (ICOON)*, (2019), pp. 1–3.
24. K. Somiya, A. G. Gurkovsky, D. Heinert, S. Hild, R. Nawrodt, and S. P. Vyatchanin, “Reduction of coating thermal noise by using an etalon,” *Phys. Lett. A* **375**, 1363–1374 (2011).
25. C. S. Embrey, J. Hordell, P. G. Petrov, and V. Boyer, “Bichromatic homodyne detection of broadband quadrature squeezing,” *Opt. Express* **24**, 27298–27308 (2016).
26. Y. Ma, H. Miao, B. H. Pang, M. Evans, C. Zhao, J. Harms, R. Schnabel, and Y. Chen, “Supplementary material for a Proposal for Gravitational-Wave Detection Beyond the Standard Quantum Limit using EPR Entanglement,” (2017).

27. R. M. Waxler and G. W. Cleek, "The Effect of Temperature and Pressure on the Refractive Index of Some Oxide Glasses," J. research Natl. Bureau Standards. Sect. A, Phys. chemistry **77A** 6, 755–763 (1973).
28. "Mephisto/Mephisto S datasheet," <https://www.coherent.com/content/dam/coherent/site/en/resources/datasheet/lasers/mephisto-mephisto-s-ds.pdf>.
29. W. Electronics, *LFI-3751 with Autotune PID - Thermoelectric Temperature Controller* (LFI3751-00400-C Rev D).
30. *SPECIFICATION OF THERMOELECTRIC MODULE AMS-71-1.0-1.5 (23 × 23) HT120 E L2 69K* (AMS Technologies).
31. "GaussianBeam," <http://gaussianbeam.sourceforge.net/>.

OPTICA
PUBLISHING GROUP
Formerly OSA